J. Electrochem. Soc. 142, 2823 (1995)

Modeling of the Kinetics of Dopant Precipitation in Silicon

Scott T. Dunham

Department of Electrical, Computer and Systems Engineering

Boston University, Boston, MA 02215

Abstract

In heavily-doped silicon, dopant aggregation leads to a reduction in the electrically active concentration. For thermal cycles typical of VLSI fabrication, the kinetics of this precipitation process can play a critical role in determining the active doping levels and thus device electrical characteristics. In this work, we develop a general kinetic precipitation model which explicitly considers the time evolution of the precipitate size density, and is thus able to account for a broad range of behavior. We compare our model to previously published experimental data for arsenic and phosphorus activation/deactivation in silicon over a wide temperature range (300 - 800°C), and find that it can account accurately for the experimental observations, including reverse annealing following a temperature step.

1 Introduction

Above a temperature-dependent concentration, substitutional silicon dopants are electrically inactive as well as immobile due to aggregation of the excess dopant into precipitates or clusters. Since electrical properties depend primarily on the active dopant concentrations, understanding and modeling of the activation process is critical for the prediction of device behavior. Despite the importance of aggregation processes, the kinetics of dopant activation are usually ignored and instead a simple solid-solubility cutoff or steady-state clustering is assumed. However, this approach cannot account for experimental observations such as active dopant concentrations above solid solubility [1, 2], doping levels above solid solubility from drive-ins [3, 4, 5], or the dependence of activation on thermal history [1, 2] and ramp-down rate [6].

In this work, we describe a general kinetic precipitation model which is able to account for thermal history effects through consideration of the evolution of the full precipitate size distribution, both above and below the critical size. We begin by describing the model and then go on to compare the model to experimental data, demonstrating that it can account for dopant activation/deactivation behavior in a consistent manner.

2 Kinetic Precipitation Model

The modeling of precipitation processes is complicated by the fact that precipitates can assume a wide range of sizes and shapes, with corresponding changes in their properties. Precipitate size plays a particularly central role as under identical conditions, precipitates of different sizes may manifest opposite behavior. For example, under typical conditions, small precipitates tend to shrink, while large precipitates grow. Thus, unlike substitutional dopants, for which it is sufficient simply to keep track of the number of dopants, to model precipitation, it is essential to distinguish between systems containing a few large precipitates versus a large number of much smaller precipitates.

Dopant activation kinetics have been addressed using "dynamic clustering" models [6, 7], but as we discuss below, these models are inconsistent with a number of the experimental observations [1, 2, 8] because they assume a single fixed cluster size rather than a range of precipitate sizes. Classical approaches to modeling of precipitation phenomena separate the system into nucleation and growth processes [9]. This approach allows a qualitative description of precipitation kinetics, but is not sufficient to address quantitatively the effects of thermal history resulting from the complex thermal cycles used in the fabrication of VLSI device structures. In order to accurately model activation/deactivation due to precipitation, it is necessary to consider the full distribution of precipitate sizes as a function of time $f_n(t)$. The general approach could be considered an extension of that used by Becker and Döring [10] for modeling of nucleation, with two major changes: consideration of the full distribution rather than forcing it to zero at some point above the critical size, and consideration of the evolution of the system with time, rather than assuming steady-state. A similar approach utilizing the Fokker-Planck equation has also been used by Brabec *et al.* [11] and Schrems *et al.* [12, 13]. As is typical, we will not consider variations in properties with changes in shape, but rather assume that the average behavior of precipitates of a given size can be approximated by that for a precipitate shape which minimizes free energy (generally spherical for small volume changes, platelets for large misfits).

2.1 Precipitate Energy

Dopant precipitation is driven by the fact that above a certain doping level (the solid solubility C^{ss}) the free energy of the system can be reduced by forming a separate dopant-rich phase. However, there is an energy barrier to forming the separate phase due to surface and strain energy associated with finite precipitates. The resulting free energy change upon precipitate formation can be written as [9]

$$\Delta G_n = -nkT \ln\left(\frac{C}{C^{ss}}\right) + \Delta G_n^{\text{excess}}, \tag{1}$$

with n the number of solute (dopant) atoms in the precipitate and C the concentration of solute. The excess energy $\Delta G_n^{\text{excess}}$ typically becomes proportional to the precipitate surface area for large sizes. However, for small precipitates, the excess energy can be expected to deviate strongly from this asymptotic behavior. Therefore, we use an expression of the form

$$\Delta G_n^{\text{excess}} = a_1 n^{m_1} + a_2 n^{m_2} \dots . \tag{2}$$

We take $m_1 > m_2 > \dots$ so that m_1 controls the asymptotic behavior and is given by the dependence of precipitate area on size (e.g., 2/3 for spheres), while the other terms modify the free energy behavior for small sizes.

In this work, we assume that the free energy is a function only of size and is independent of temperature. However, it should be noted that changes in strain relaxation or point defect interactions with temperature may lead to the free energies changing with temperature, and some of the differences that do exist between the experimental data and model predictions may be due to such effects.

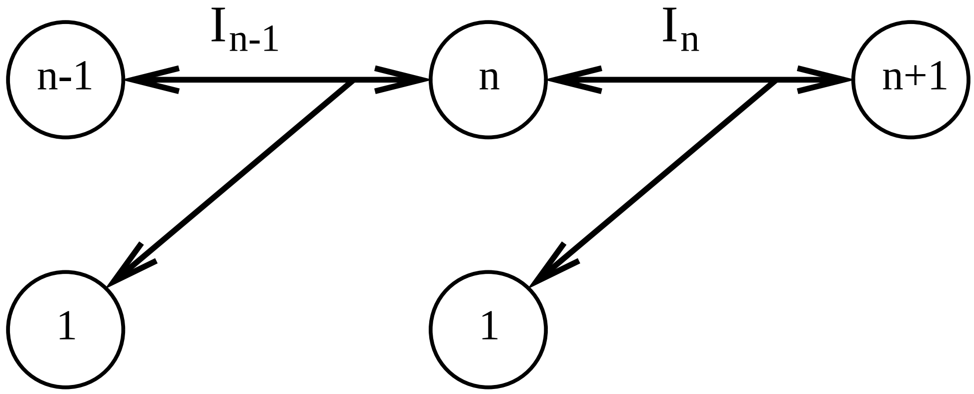

Figure 1: *Precipitates grow or shrink by absorbing or emitting solute atoms.*

2.2 Evolution of Precipitate Size Distribution

Rather than separating the precipitation process into separate nucleation and growth processes, we consider the evolution of the full precipitate size distribution, thus keeping essential information about the effects of previous thermal history which is critical to predicting future behavior. The precipitation process proceeds by the addition of solute atoms to existing precipitates, resulting in the generation of a size $n+1$ precipitate from a size n precipitate and a solute atom (Figure 1). The evolution of the precipitate density can thus be described by a series of rate equations for each precipitate size:

$$\frac{df_n}{dt} = I_{n-1} - I_n, \quad n \geq 2, \tag{3}$$

where I_n is the rate of growth from size n to $n+1$. Additional terms must be considered for the solute atoms, since they are involved in the growth of precipitates of all sizes (including the formation of a size two precipitate through the combination of two solute atoms,

$$\frac{dC}{dt} = \frac{df_1}{dt} = -2I_1 - \sum_{n=2}^{\infty} I_n \tag{4}$$

A diffusion term could also be included for the solute atoms (precipitates of size two and larger are assumed to be immobile); however, in this work we only compare the model to systems which can be assumed to be approximately homogeneous in space.

The flux in precipitate size space from size n to size $n+1$ is given by the difference between the rate at which size n precipitates are growing to size $n+1$ minus the rate at which size $n+1$ precipitates are dissolving:

$$I_n = g_n f_n - d_{n+1} f_{n+1}. \tag{5}$$

For a reaction-limited precipitation process, the growth rate g_n is given by:

$$g_n = A_n k_n C, \tag{6}$$

where A_n is the active precipitate interface area, k_n is the interface reaction rate, and C is the solute concentration The dissolution rate can them be calculated based on the fact that in equilibrium the net flux I_n is zero:

$$d_{n+1} = A_n k_n C_n^*, \tag{7}$$

where

$$C_n^* = C \exp\left(-\frac{\Delta G_{n+1} - \Delta G_n}{kT}\right) = C^{ss} \exp\left(-\frac{\Delta G_{n+1}^{\text{excess}} - \Delta G_n^{\text{excess}}}{kT}\right) \tag{8}$$

is defined to be the solute concentration for which there is no change in energy with the transition from size n to $n+1$ ($\Delta G_{n+1} = \Delta G_n$).

2.3 Solute Diffusion

The analysis above assumed that the precipitation process was reaction-limited; however, particularly for large precipitates, the process is more often diffusion-limited and the concentration of solute atoms near a growing or shrinking precipitate is different than the concentration far away from any precipitates. This will be particularly important when the net growth or dissolution rate is high. Therefore, we include both the interface reaction rate as well as the solute diffusivity in our analysis. The simplest approach to estimating the growth and dissolution rates is to assume that the solute distribution near a precipitate can be approximated by the steady-state distribution for the current precipitate size and net growth rate. Solving the steady-state diffusion equation in spherical coordinates gives:

$$C_n^i - C^\infty = \frac{C_n^* - C^\infty}{1 + D/k_n r_n}, \tag{9}$$

where r_n is the precipitate radius, C_n^i is the solute concentration near the precipitate matrix interface and $C^\infty = f_1$ is the bulk solute concentration. The resulting expected net growth rate for any single precipitate of size n is

$$\frac{dn}{dt} = \frac{A_n D(C^\infty - C_n^*)}{r_n + D/k_n} = g_n - d_{n+1}. \tag{10}$$

Since the growth rate should be directly proportional to the solute concentration, while the dissolution rate must be independent of the solute concentration, we can separate Equation (10) to give:

$$g_n = \frac{A_n D C^\infty}{r_n + D/k_n} \tag{11}$$

and

$$d_{n+1} = \frac{A_n D C_n^*}{r_n + D/k_n}. \tag{12}$$

The new effective reaction rate is

$$\frac{D}{r_n + D/k_n} = \frac{(D/r_n)k_n}{k_n + D/r_n}, \tag{13}$$

which is just the series combination of the rate of diffusion to the precipitate (D/r_n) and the interface reaction rate (k_n).

The fact that the solute concentration in the neighborhood of a growing or shrinking precipitate can differ substantially from the far-field concentration (C^∞), might lead one to conclude that the average solute concentration (as determined by measuring the active doping density) would also deviate substantially from the far-field concentration (which determines the evolution of the size distribution). However, the effective far-field concentration seen by any one precipitate is actually the superposition of the diffusion fields of all the other precipitates. Thus, as long as the precipitate density is large, the far-field solute concentration remains well approximated by the average solute concentration.

To account for the variation of diffusivity with active doping level, we use:

$$D \cong D^0 + D^- (n/n_i) + D^{\mathrm{H}} (C/C_{\mathrm{ref}})^{n_H}, \tag{14}$$

where $C = f_1$ is the bulk active doping level. The first two terms are the standard Fermi level dependent diffusivity, while the last term accounts for the rapid increase in diffusivity observed above about $2 \times 10^{20}\mathrm{cm}^{-3}$ for group IV and V elements [14] ($n_H \cong 4.5$ for As). This rapid increase of diffusivity with doping level can be attributed to the interaction of vacancies with more than one dopant atom, leading to a reduction in the activation energy for dopant/vacancy pair motion [15, 16, 17]. This effect is particularly significant for deactivation studies as the active doping level can be well above the solid solubility.

2.4 Transient Solute Distributions

For long-time anneals at a single temperature, the steady-state assumption for the diffusion field around a precipitate is a reasonable approximation. However, when the temperature is changed, the solute distribution cannot respond instantaneously to the new steady-state distribution. To address this issue we use a more general analysis in this work. We approximate the distribution of solute atoms in the neighborhood of the precipitate by the distribution that would be present if the precipitate had always been its current size, but do not assume steady-state.

By applying analyses from solid-state heat conduction [18], we are able to calculate the interface solute concentration in the general case of both diffusion and interface limited processes to be

$$C_n^i - C^\infty = \frac{C_n^* - C^\infty}{1 + D/k_n r_n} + \left[C^i(0) - C^i(\infty)\right] \exp\left({h'_n}^2 Dt\right) \operatorname{erfc}\left(h'_n \sqrt{Dt}\right), \tag{15}$$

where $h'_n = k/D + 1/r$ and $C^i(0)$ and $C^i(\infty)$ are the interface concentrations at time $t = 0$ and in steady-state, respectively. For long times ($h'_n \sqrt{Dt} \gg 1$), the second term vanishes, reducing Equation (15) to the steady-state expression. Since the steady-state solution changes whenever the temperature changes, time is reinitialized for each change in temperature. In deriving this expression, we assumed that the initial solute distribution in the neighborhood of the precipitate can be approximated by the $1/r$ dependence on distance of steady-state distributions and estimate the value of $C^i(0)$ to approximate the current solute distribution whenever the temperature is changed. Due to the strong dependence of D on the solute concentration, $\int D\,dt$ is actually used in place of Dt in Equation (15).

2.5 Rediscretization for Large Sizes

If large precipitates are to be considered, the full system described by Equations (3) and (4) quickly becomes very large. For example, to consider precipitates up to a radius of 200 Å would require more than 10^6 equations. In order reduce the number of equations, for larger precipitate sizes we consider the system to be nearly continuous and rediscretize the size distribution more coarsely, where now each point in the distribution can represent a range

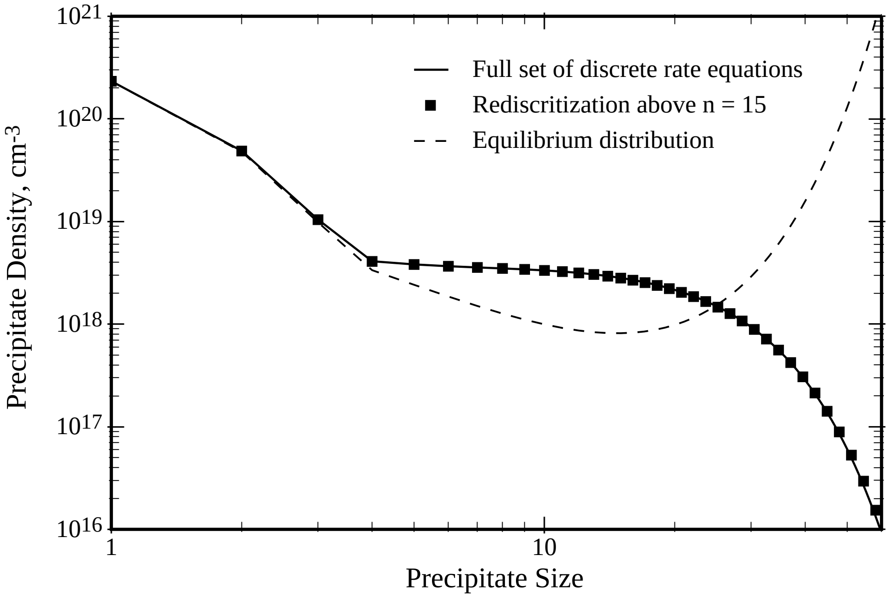

Figure 2: Comparison of precipitate size distribution calculated for rediscritized distribution to the results of solving the full set of discrete rate equations.

of sizes rather than just a single size. Thus we replace n with $n[i]$ where $f_{n[i]}$ represents the concentrations between sizes $(n[i-1]+n[i])/2$ and $(n[i]+n[i+1])/2$. To ensure a smooth transition between small sizes, where the discrete nature of the problem is critical, to larger sizes, where we can use the rediscritization, we generalize Equation (5) to represent the flux at a fictitious size halfway between $n[i]$ and $n[i+1]$:

$$\begin{aligned} I_{n[i]} = \frac{1}{2}\Big\{ &\left[\left(g_{n[i]} + dn[i]\right) f_{n[i]} - \left(g_{n[i+1]} + dn[i+1]\right) f_{n[i+1]}\right] / (n[i+1] - n[i]) \\ &+ \left[\left(g_{n[i]} - dn[i]\right) f_{n[i]} + \left(g_{n[i+1]} - dn[i+1]\right) f_{n[i+1]}\right]\Big\}. \end{aligned} \tag{16}$$

Note that if $n[i+1] = n[i]+1$, Equation (16) reduces to Equation (5). As confirmation of the effectiveness of the rediscretization, we obtain simulation results which are very close to those from the solution of the full set of discrete equations (Figure 2).

2.6 Point Defect Interactions

In general, formation of a precipitate phase also involves a change in volume. There are two ways in which such volume changes can be accommodated: lattice strain and point defect interactions. Strain energy has already been included in the $\Delta G_n^{\text{excess}}$ term. However, the emission or absorption of point defects (interstitials and vacancies) can greatly reduce the strain energy resulting from volume differences. For example, a precipitate phase with a larger volume than the matrix might incorporate vacancies. Thus, given the bulk vacancy density, there will be some number of incorporated vacancies which minimizes the system free energy – balancing point defect interactions with strain relaxation. The resulting free energy for formation of a precipitate with n solute atoms, $n_{\rm V}$ vacancies and $n_{\rm I}$ interstitials is then

$$\Delta G_n = -nkT\ln\left(\frac{C}{C^{ss}}\right) - n_{\rm V}kT\ln\left(\frac{C_{\rm V}}{C_{\rm V}^*}\right) - n_{\rm I}kT\ln\left(\frac{C_{\rm I}}{C_{\rm I}^*}\right) + \Delta G_n^{\text{excess}}, \tag{17}$$

where C^{ss} is the solubility when $C_{\mathrm{V}} = C_{\mathrm{V}}^{*}$ and $C_{\mathrm{I}} = C_{\mathrm{I}}^{*}$.

Recent experiments suggest that arsenic precipitation involves the absorption of vacancies and/or emission of interstitials as arsenic deactivation is enhanced during vacancy injection and retarded during interstitial injection [19]. However, in this work we consider only activation in near-surface regions during inert-ambient anneals and neglect any effects due to nonequilibrium point defect concentrations.

3 Comparison to Experiments

We have conducted a series of simulations utilizing the model described above, and we find that the model is able to predict observed dopant activation/deactivation behavior, including effects that are inconsistent with both standard clustering, as well as classical nucleation and growth models. For each dopant, the full set of experimental data was fit using a single set of parameters with PROFILE [20], a Levenberg-Marquardt nonlinear optimization code.

Whenever possible, we use parameter values determined from experimental data which is independent of precipitation kinetics. For dopant diffusivity, we use activated coefficients (e.g., $D^0 = Q_{D^0}\exp(-E_{D^0}/kT)$) based on published arsenic diffusivity data [14, 21] or our recent work on phosphorus diffusion [22]. However, there is very limited data with which to characterize the diffusion behavior at very high doping levels as included in the last term in Equation (14). For arsenic, we retain the activation energy as a fitting parameter, while matching the experimental measurements at 1050°C [14]. For phosphorus, there is no reliable data for doping levels above $2 \times 10^{20}\mathrm{cm}^{-3}$, so both the activation energy and pre-exponential factor are characterized based on the activation/deactivation kinetics. For solid solubility, we use temperature activated expressions derived from published data [3, 23, 24, 25, 26]. We assume that the barrier for hopping of a dopant atom to a site adjacent to a precipitate is the same as the bulk hopping barrier so that $k_n = D/\lambda$, where D is the diffusivity and λ is the lattice spacing.

3.1 Experimental Data Set

To test the precipitation model, we use experimental data from Nobili *et al.* [1, 2]. The test structures were generated by implanting arsenic or phosphorus into silicon and laser annealing to activate all the dopant. The samples were then annealed and the deactivation kinetics were observed, with the active doping concentrations measured using resistivity and Hall measurements, combined with anodic oxidation and etching. Two basic types of annealing schedules were used: isochronal anneals, which consisted of a series of 1 h anneals, with the temperature increased at each step, and two-step anneals, which involved a series of anneals at one temperature, followed by a subsequent set of anneals at a higher temperature.

The resulting doping profiles are box-like [1, 2] and thus we approximate the doping distributions by square profiles, with depths as measured experimentally. We neglect broadening of the profiles during annealing due to the low temperatures (≤ 800°C) used. By integrating the total dopant motion during these anneals, we were able to confirm that ignoring profile broadening was an excellent approximation.

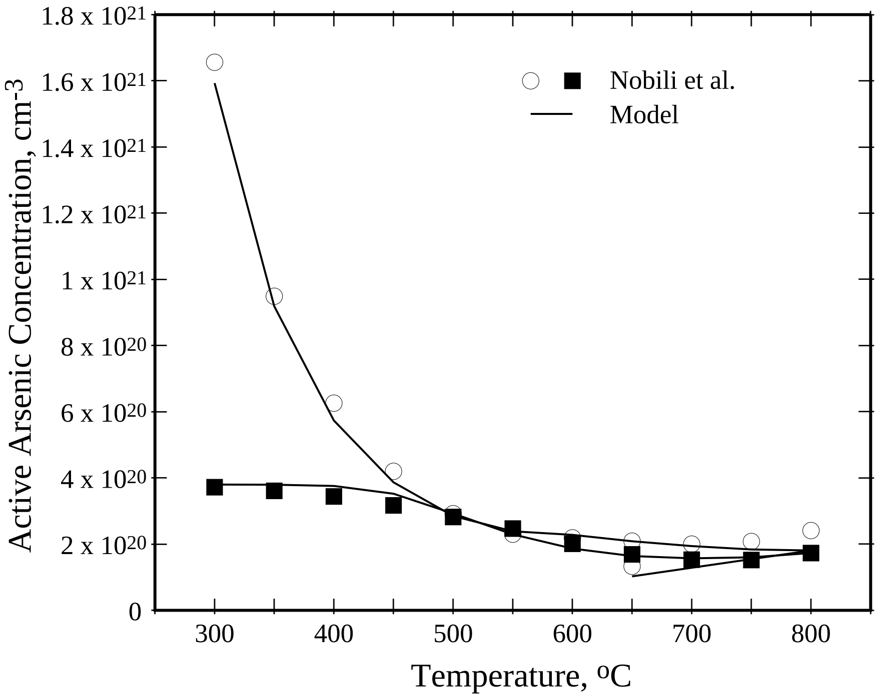

Figure 3: *Peak active arsenic concentration for isochronal annealing of implants with initial peak doping concentrations of* $3 \times 10^{21}\mathrm{cm}^{-3}$ *and* $4 \times 10^{20}\mathrm{cm}^{-3}$. *Experimental results are from Nobili et al. [1]. The lower point at 650°*C *is for an additional 30 h anneal following the last isochronal anneal at 800°*C.

3.2 Arsenic Isochronal Anneals

Figure 3 shows the comparison of the model to isochronal arsenic annealing data of Nobili *et al.* [1] for two different implant doses. The samples were annealed for 1h at each temperature from 300°C to 800°C in 50°C steps. It can be seen that the model does an excellent job of accounting for the experimental observations. Both the model and the data manifest much more rapid precipitation for the higher dose. This is because the critical size, and thus the maximum activation barrier to form critical nuclei, decrease with supersaturation. In fact, both the data and the model have a slightly retrograde regime near 550°C, where the higher total dose actually has a lower active concentration. Following the last isochronal anneal at 800°C, the high-dose sample was subsequently annealed for 30h at 650°C, demonstrating that the system remains well above solid solubility.

3.3 Arsenic Two-Step Anneals

Figure 4 shows the striking behavior observed for a two-step anneal. The active doping was first monitored during a 32 h anneal at 650°C and then the temperature was raised to 750°C as the annealing continued. Despite the fact that the active doping remained far above solid solubility (1.1×10^{20} at 750°C) the precipitation process initially reversed itself following the temperature step before eventually continuing at the faster rate characteristic of the higher temperature. The model accurately replicated this behavior and examining the model solution illuminates the causes of this unusual reverse annealing process.

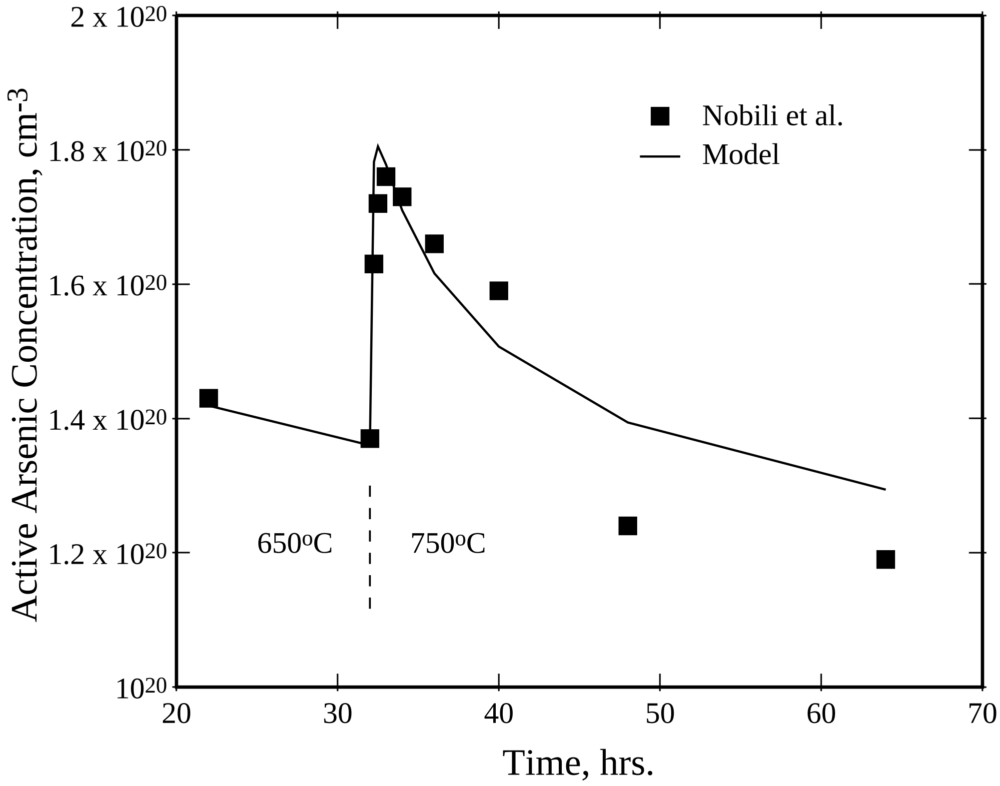

Figure 4: *Peak active arsenic concentration versus time for two-step anneal first at 650°C for 32h and then at 750°C. Initial peak doping is* $9 \times 10^{20}\text{cm}^{-3}$. *Experimental data from Nobili et al. [1].*

Figure 5 shows precipitate densities before and after the temperature step. Upon increasing the temperature from 650 to 750°C, the solid solubility increases, reducing the supersaturation and thus the critical precipitate size. Therefore, precipitates which previously were growing, now shrink and disappear. The result is an initial increase in the active doping concentration. In contrast, the precipitates which remain stable continue to grow and eventually dominate leading to dopant deactivation at longer times. It may be noted that this type of behavior (reverse and then forward annealing) is only possible when there is a distribution of precipitate sizes such that some shrink while others grow, rather than a single dominant precipitate size as assumed in clustering models.

3.4 Phosphorus Precipitation Kinetics

We have found similar agreement between experiments and simulations for other dopants [27]. As an example, Figure 6 shows a comparison to data from Nobili *et al.* [2] for a series of isochronal anneals of laser-annealed phosphorus implants. The experimental conditions are similar that for the arsenic data, with 1 h anneals at 25°C steps from 300 to 750°C. Both experiments and simulations also manifest the reverse annealing upon temperature increase as for arsenic [2, 27].

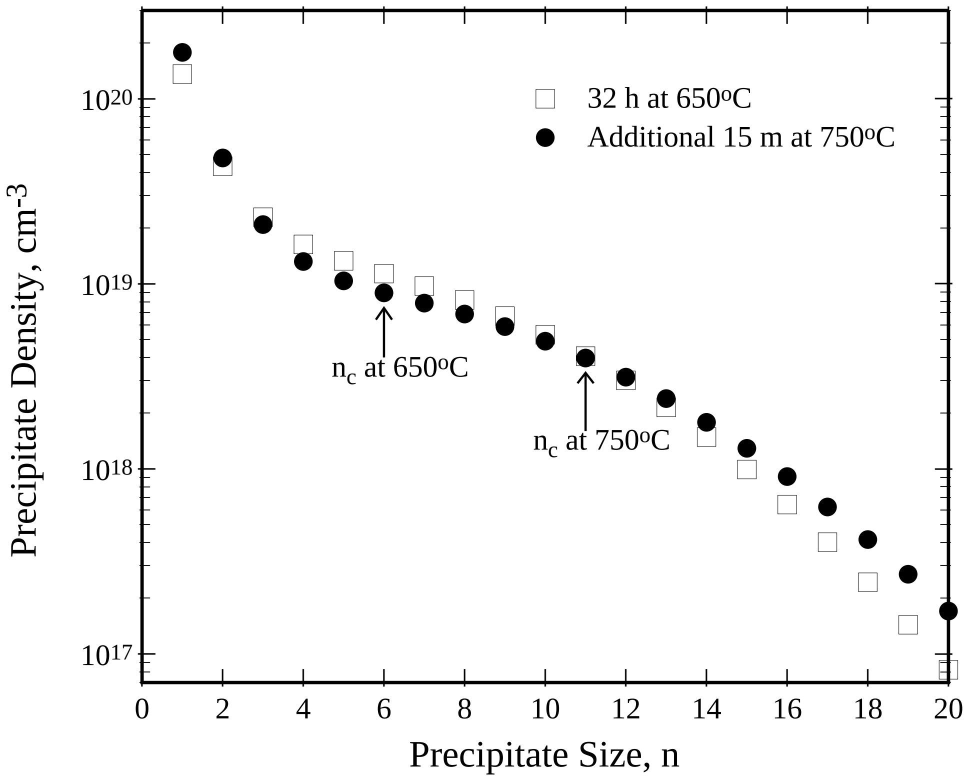

Figure 5: *Simulated precipitate size distribution at the end of a 32 h anneal at 650°*C *and after a subsequent 15 min anneal at 750°*C.

3.5 Deactivation Below Solid Solubility

Since the model considers subcritical as well as stable precipitates (in contrast to classical nucleation and growth models), it also accounts for incomplete activation for concentrations below solid solubility as observed for arsenic and boron. Figure 7 shows simulated active arsenic concentration following a 6 h anneal at 800°C versus the total arsenic doping level. At doping levels close to, but below solid solubility, not all of the arsenic is active due to the presence of a significant density of subcritical clusters. Such observations are often used to justify the use of clustering rather than precipitation models. The density of these clusters depends strongly on the dependence of energy on size in this regime, and in fact, clustering models can be considered a subset of the more general analysis considered here, with the precipitate energy assumed to be large for all sizes except the dominant cluster size.

Above solid solubility, the active concentration levels off due to precipitation. (There is a small peak in active doping due to the faster kinetics at higher supersaturations.) This is as observed experimentally [1, 2], but is in contrast with clustering models, for which the active concentration continues to increase with doping level.

4 Conclusions

In summary, we have developed a model for the kinetics of dopant precipitation and applied it to dopant deactivation during annealing following implant and laser anneal. The model considers the time evolution of the full precipitate size distribution and thus accounts

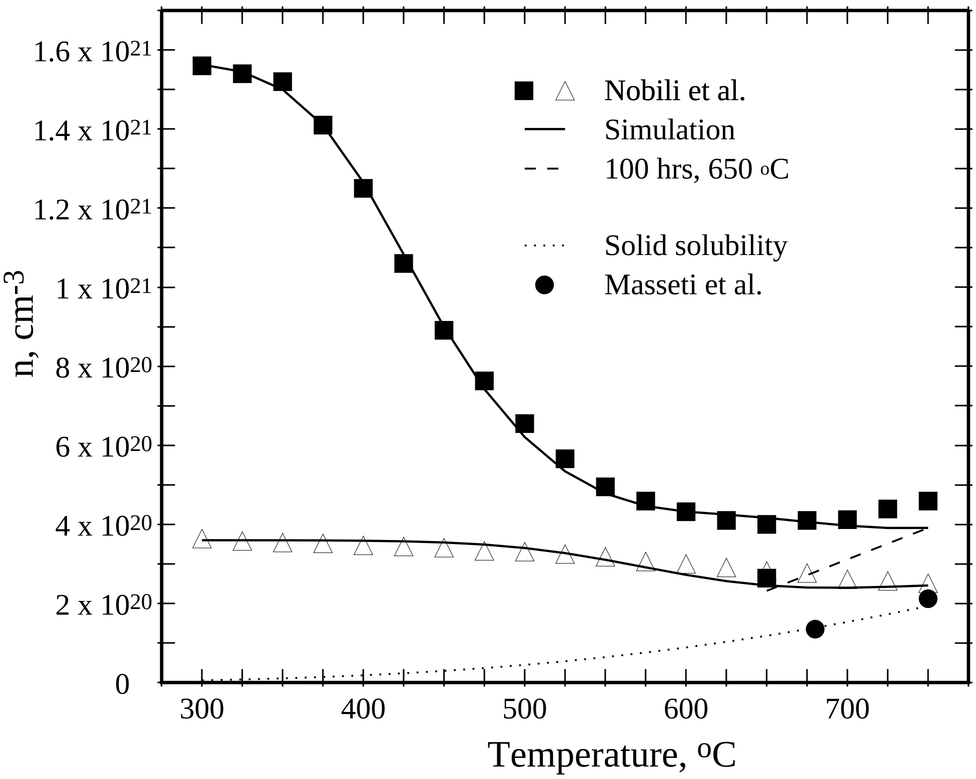

Figure 6: *Peak active phosphorus concentration for isochronal annealing of implants with two different initial doping levels compared to kinetic precipitation model. Experimental results are from Nobili et al. [2]. Also shown for comparison are solid solubility data from Masetti et al. [3].*

for experimental observations which have previously been associated with either clustering or classical precipitation models. Because the model does not assume a steady-state solute distribution in the neighborhood of growing/shrinking precipitates, we are able to more effectively model transient behavior following changes in temperature. We show that our kinetic precipitation model can account for the kinetic activation/deactivation behavior observed for silicon dopant species over a wide range of temperatures in a consistent manner. In particular, the simulations account for isochronal annealing as a function of doping level for both arsenic and phosphorus over the temperature range of 300 – 800°C, as well as the transient reverse annealing effects observed during multiple step anneals with increasing temperature.

Acknowledgements

This work was supported by SRC/SEMATECH grants #91-MC-503 and #93-MJ-530.

References

[1] D. Nobili, A. Carabelas, G. Celotti and S. Solmi, *J. Electrochem. Soc.* **130**, 922 (1983).

[2] D. Nobili, A. Armigliato, M. Finetti and S. Solmi, *J. Appl. Phys.* **53**, 1484 (1982).

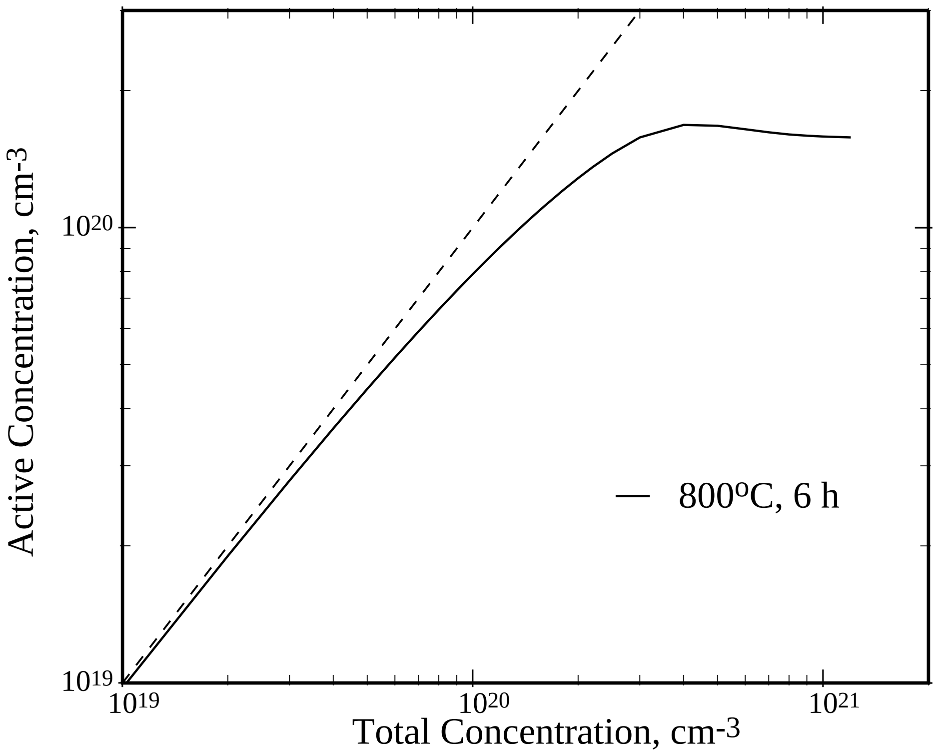

Figure 7: *Simulated active versus total arsenic concentration following 6 h anneal at 800°C. Also shown for reference is dotted line representing full activation.*

[3] G. Masetti, D. Nobili and S. Solmi, in **Semiconductor Silicon**, eds. H. R. Huff and E. Sirtl (Electrochemical Society Proc. **77-2**, Pennington, NJ, 1977) p. 648.

[4] P. Negrini, D. Nobili and S. Solmi, *J. Electrochem. Soc.* **122**, 1254 (1975).

[5] R. B. Fair and J. C. C. Tsai, *J. Electrochem. Soc.* **124**, 1107 (1977).

[6] M. Orlowski, R. Subrahmanyan and G. Huffman, *J. Appl. Phys.* **71**, 164 (1992).

[7] M. Y. Tsai, F. F. Morehead and J. E. E. Baglin, *J. Appl. Phys.* **51**, 3230 (1980).

[8] P. M. Rousseau, P. B. Griffin, P. G. Carey and J. D. Plummer, in **Process Physics and Modeling**, eds. G. R. Srinivasan, K. Taniguchi and C. S. Murthy (Electrochem. Soc. Proc. **93-6**, Pennington, NJ, 1993) p. 130.

[9] J. W. Christian in **The Theory of Transformations in Metals and Alloys, Part I, 2nd ed.**, (New York, Pergamon Press, 1981).

[10] Becker and Döring, *Ann. d. Phys.* **24**, 719 (1935).

[11] T. Brabec, M. Schrems, M. Budil, H. W. Pötzl, W. Kuhnert, P. Pongratz, G. Stingender and M. Grasserbauer, *J. Electrochem. Soc.* **136**, 1542 (1989).

[12] M. Schrems, T. Brabec, M. Budil, H. Pötzl, E. Guerrero and D. Hüber, *Mat. Sci. Eng.* **B4**, 393 (1989).

[13] M. Schrems, P. Pongratz, M. Budil, H. Pötzl, J. Hage, E. Guerrero and D. Hüber.

[14] A. N. Larsen, K. K. Larsen, P. E. Andersen and B. G. Svensson, *J. Appl. Phys.* **73**, 691 (1993).

[15] D. Mathiot and J. C. Pfister, *J. Phys. Lett.* **43**, 453 (1982).

[16] S. T. Dunham and C. D. Wu, in **NUPAD '94** (IEEE, Piscataway, NJ, 1994).

[17] S. T. Dunham and C. D. Wu, in review.

[18] H. S. Carslaw and J. C. Jaeger, in **Conduction of Heat in Solids,** 2^{nd} **ed.** (Oxford, Clarendon Press, 1959).

[19] R. Subrahmanyan, M. Orlowski and A. R. Sitaram, in **Process Physics and Modeling**, eds. G. R. Srinivasan, K. Taniguchi and C. S. Murthy (Electrochem. Soc. Proc. **93-6**, Pennington, NJ, 1993) p. 120.

[20] G. J. L Ouwerling, *The PROFILE/PROF2D User's Manual*, Delft University of Technology, 1987.

[21] R. B. Fair, in **Impurity Doping Processes in Silicon**, ed. F. F. Y. Yang (North-Holland, New York, 1981) p. 315.

[22] F. Wittel and S. T. Dunham, in review.

[23] A. Leitoila, J. F. Gibbons and T. Sigmon, *Appl. Phys. Lett.* **36**, 765 (1980).

[24] R. Angelucci, A. Armigliato, E. Landi, D. Nobili and S. Solmi, **1987 ESSDERC Proceedings**, p. 461.

[25] J. L. Hoyt and G. F. Gibbons, in Rapid Thermal Processing, eds. T. O. Sedgwick, T. E. Seidel and B.-Y. Tsaur (Materials Research Society Proceedings **52**, Pittsburgh, PA, 1986) p. 15.

[26] M. Derdour, D. Nobili and S. Solmi, *J. Electrochem. Soc.* **138**, 857 (1991).

[27] S. T. Dunham, Electrochemical Society Extended Abstracts, Vol. **92-1**, St. Louis, MO, May 1992.